Dynamical construction of quadrupolar and octupolar topological superconductors

Arnob Kumar Ghosh [1,2,*] Tanay Nag [3,†] and Arijit Saha [1,2,‡]

[1]*Institute of Physics, Sachivalaya Marg, Bhubaneswar 751005, India*

[2]*Homi Bhabha National Institute, Training School Complex, Anushakti Nagar, Mumbai 400094, India*

[3]*Institut für Theorie der Statistischen Physik, RWTH Aachen University, Aachen 52056, Germany*

(Received 26 January 2022; revised 21 March 2022; accepted 29 March 2022; published 11 April 2022)

We propose a three-step periodic drive protocol to engineer two-dimensional (2D) Floquet quadrupole superconductors and three-dimensional (3D) Floquet octupole superconductors hosting zero-dimensional Majorana corner modes (MCMs), based on unconventional d-wave superconductivity. Remarkably, the driven system conceives four phases with only zero MCMs, no MCMs, only anomalous π MCMs, and both regular zero and anomalous π MCMs. To circumvent the subtle issue of characterizing zero and π MCMs separately, we employ the periodized evolution operator to architect the dynamical invariants, namely quadrupole and octupole motion in 2D and 3D, respectively, that can distinguish different higher-order topological phases unambiguously. Our study paves the way for the realization of dynamical quadrupolar and octupolar topological superconductors.

DOI: 10.1103/PhysRevB.105.155406

I. INTRODUCTION

Topological superconductors (TSCs) hosting Majorana zero modes (MZMs) have been the cornerstone for the last two decades due to their potential application in topological quantum computations utilizing non-Abelian statistics [1–4]. The quest for TSC emerges following the elegant proposal by Kitaev [1], and the idea by Fu and Kane [5] that emphasized the realization of MZMs on the two-dimensional (2D) surface of a three-dimensional (3D) topological insulator (TI), in proximity to an s-wave superconductor and magnetic insulator. Very recently, the advent of generalized bulk boundary correspondence (BBC) in the higher-order topological (HOT) phase [6–19] has made the field more exciting. An nth-order HOT insulator [superconductor (HOTSC)] phase is characterized by the existence of electronic (Majorana) boundary modes at their $(d-n)$-dimensional boundaries $(0<n\leqslant d)$ [20–46].

To this end, we focus on the periodically driven quantum systems, exhibiting nontrivial properties compared to their static counterparts such as dynamical localization [47–49], many-body localization [50–52], Floquet time crystals [53,54], higher harmonic generation [55,56], etc. In particular, anomalous boundary modes at finite quasienergy, namely π modes, with concurrent regular zero modes, can be engineered by Floquet driving [57]. Moreover, one can architect the Floquet HOT insulators (FHOTIs) [58–76] and Floquet HOT superconductors (FHOTSCs) [77–82] out of nontopological or lower-order topological systems.

To date, there exist a very few proposals, based on a steplike protocol, to realize the FHOTI phase hosting both zero and anomalous π modes [64,65,72,74]. The dynamical FHOTI modes in 2D are characterized by redefining the polarization for driven systems, where the mirror symmetry plays a pivotal role [64]. The hunt for such FHOTSC phases is still in its infancy [82], along with their dynamical topological characterizations. Hence, we seek the answers to the following intriguing questions: (1) Is it possible to systematically generate the FHOTSC hosting both zero and the anomalous π-Majorana modes in 2D and 3D? (2) How can we characterize these zero and π modes using a proper dynamical topological invariant?

In this paper, we employ a periodic step-drive protocol to systematically formulate a 2D quadrupolar Floquet second-order TSC (FSOTSC) and a 3D octupolar Floquet third-order TSC (FTOTSC), based on an unconventional d-wave superconductor. This driving protocol allows us to realize and characterize both the zero and π Majorana corner modes (MCMs), and serves as the primary motivation of the current work. We extensively study the dynamical octupolar motion in 3D, which adds significant merit to the problem we are dealing with.

The remainder of the paper is organized as follows. We discuss the generation of anomalous Majorana modes in Sec. II. We topologically characterize the 2D FSOTSC and 3D FTOTSC phase using a dynamical quadrupole moment and dynamical octupole moment, respectively, in Sec. III. Finally, we summarize and conclude our paper in Sec. IV.

II. GENERATION OF ANOMALOUS MAJORANA MODES

Considering the d-wave superconductor, we prescribe the following three-step drive protocol to foster the 2D FSOTSC and 3D FTOTSC:

$$\begin{aligned} H_{d\mathrm{D}}(\mathbf{k},t) &= J_1' h_{1,d\mathrm{D}}(\mathbf{k}), \quad t\in[0,T/4],\\ &= J_2' h_{2,d\mathrm{D}}(\mathbf{k}), \quad t\in(T/4,3T/4],\\ &= J_1' h_{3,d\mathrm{D}}(\mathbf{k}), \quad t\in(3T/4,T]. \end{aligned} \tag{1}$$

*arnob@iopb.res.in
†tnag@physik.rwth-aachen.de
‡arijit@iopb.res.in

Here, $J_i' h_{i,dD}(\mathbf{k})$ denotes the Hamiltonian of the system at the ith step in d dimensions (dD), while J_1' and J_2' carry the dimensions of energy. We define the dimensionless parameters $(J_1, J_2) = (J_1'T, J_2'T)$, where T $(\Omega = 2\pi/T)$ represents the time period (frequency) of the drive. We set $\hbar = c = 1$. In particular, to generate a 2D FSOTSC, we choose $h_{1,2D}(\mathbf{k}) = h_{3,2D}(\mathbf{k}) = \tau_z\sigma_z$ and $h_{2,2D}(\mathbf{k}) = \epsilon_{2D}(\mathbf{k})\tau_z\sigma_z + \Lambda_{2D}(\mathbf{k}) + \Delta_{2D}(\mathbf{k})$, whereas in 3D we consider $h_{1,3D}(\mathbf{k}) = h_{3,3D}(\mathbf{k}) = \tau_z\sigma_z$ and $h_{2,3D}(\mathbf{k}) = \epsilon_{3D}(\mathbf{k})\tau_z\sigma_z + \Lambda_{3D}(\mathbf{k}) + \Delta_{3D}(\mathbf{k})$ with $\epsilon_{2D}(\mathbf{k}) = (\cos k_x + \cos k_y)$, $\Lambda_{2D}(\mathbf{k}) = \sin k_x\tau_z\sigma_x s_z + \sin k_y\tau_z\sigma_y$, $\Delta_{2D}(\mathbf{k}) = \Delta(\cos k_x - \cos k_y)\tau_x$, $\epsilon_{3D}(\mathbf{k}) = (\cos k_x + \cos k_y + \cos k_z)$, $\Lambda_{3D}(\mathbf{k}) = \sin k_x\tau_z\sigma_x s_x + \sin k_y\tau_z\sigma_x s_y + \sin k_z\tau_z\sigma_x s_z$, and $\Delta_{3D}(\mathbf{k}) = \Delta_1(\cos k_x - \cos k_y)\tau_x + \Delta_2(2\cos k_z - \cos k_x - \cos k_y)\tau_y$. Here, $\epsilon_{dD}(\mathbf{k})$ and $\Lambda_{dD}(\mathbf{k})$ encapsulate all the hoppings and spin-orbit coupling terms in dD, respectively. In 2D, we use the $d_{x^2-y^2}$ pairing, given by $\Delta_{2D}(\mathbf{k})$ [23,81], while in 3D we incorporate mixed pairing $d_{x^2-y^2} + id_{3z^2-r^2}$, represented by $\Delta_{3D}(\mathbf{k})$ [46,83]. In the first and last step of the drive, the Hamiltonian contains only an on-site term $[h_{1,dD}(\mathbf{k})]$, providing us further analytical sophistication and facilitating the topological characterizations [57,64]. Here, both $h_{1,dD}(\mathbf{k})$ and $h_{2,dD}(\mathbf{k})$ respect the antiunitary particle-hole, unitary chiral, and mirror symmetry while the last one plays the decisive role.

The Floquet operator $U(\mathbf{k}, T)$, following the time-ordered (TO) notation, is given as [84]

$$U_{dD}(\mathbf{k}, T) = \mathrm{TO}\exp\left[-i\int_0^T dt\, H_{dD}(\mathbf{k}, t)\right]. \tag{2}$$

Using the eigenvalue equation for $U_{dD}(\mathbf{k}, T)$, $U_{dD}(\mathbf{k}, T)|\Psi\rangle = \exp[-iE(\mathbf{k})]|\Psi\rangle$, we obtain

$$E(\mathbf{k}) = \pm\arccos\{\cos[\alpha_{dD}(\mathbf{k})J_1/2]\cos[\beta_{dD}(\mathbf{k})J_2/2] - \sin[\alpha_{dD}(\mathbf{k})J_1/2]\sin[\beta_{dD}(\mathbf{k})J_2/2]\chi_{dD}(\mathbf{k})\}, \tag{3}$$

where $\alpha_{dD}(\mathbf{k}) = |h_{1,dD}(\mathbf{k})| = |h_{3,dD}(\mathbf{k})|$, $\beta_{dD}(\mathbf{k}) = |h_{2,dD}(\mathbf{k})|$, and $\chi_{dD}(\mathbf{k}) = \frac{\epsilon_{dD}(\mathbf{k})}{\alpha_{dD}(\mathbf{k})\beta_{dD}(\mathbf{k})}$. We invoke the band-gap closing across $E(\mathbf{k}) = 0, \pm\pi$ at $(k_x, k_y) = (0, 0)$ or (π, π) for 2D and at $(k_x, k_y, k_z) = (0, 0, 0)$ or (π, π, π) for 3D to acquire the generalized topological phase boundary akin to our driving protocol in d dimensions as [74]

$$\frac{d|J_2|}{2} = \frac{|J_1|}{2} + n\pi, \tag{4}$$

where $n \in \mathbb{Z}$. We show the topological phase diagram in the J_1-J_2 plane for 2D (3D) in Fig. 1(a) [Fig. 2(a)]. The phase diagram can be divided into four segments: region 1 (R1) with only zero modes, region 2 (R2) without any modes, region 3 supporting only π modes, and region 4 (R4) allowing both zero and π MCMs to coexist.

Having perceived the problem analytically, we anchor our findings with numerical results. The 2D FSOTSC and 3D FTOTSC can be identified by the presence of zero-dimensional (0D) MCMs [45]; these are computed for both regular and anomalous modes while diagonalizing the Floquet operator [Eq. (2)] with an open boundary condition (OBC) in all directions. The corresponding local density of states (LDOS) of MCMs is shown in Figs. 1(b) and 2(b), respectively, for a 2D square and 3D cubic lattice. We portray the

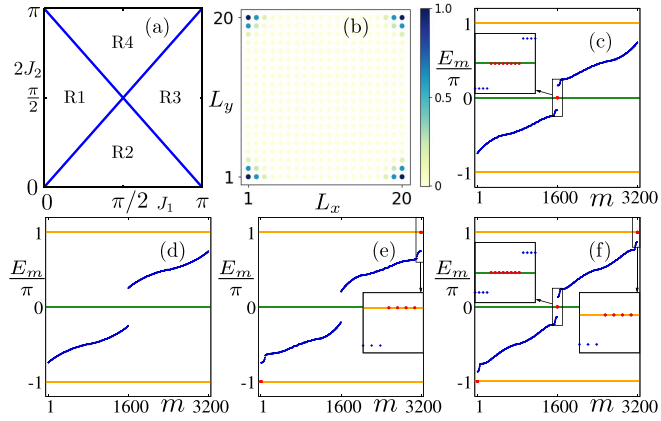

FIG. 1. (a) We depict the phase diagram of 2D FSOTSC in the J_1-J_2 plane [Eq. (4)]. (b) The LDOS is demonstrated for a 2D square lattice of dimension $L_x \times L_y$ for $E_m = 0, \pm\pi$. The quasienergy spectra E_m, computed from Eq. (2), are shown as a function of the state index m in (c)–(f) for R1–R4, respectively. We use the parameters as $(J_1, 2J_2) = [(\frac{\pi}{4}, \frac{\pi}{2}), (\frac{\pi}{2}, \frac{\pi}{4}), (\frac{3\pi}{4}, \frac{\pi}{2}), (\frac{\pi}{2}, \frac{3\pi}{4})]$ for R1–R4, respectively. We choose $\Delta = 1.0$ throughout our numerical analysis.

quasienergy spectra (E_m) for R1 (eight zero MCMs), R2 (no MCMs), R3 (four MCMs each at $E_m = \pm\pi$), and R4 (eight MCMs at $E_m = 0$ and four MCMs each at $E_m = \pm\pi$) in Figs. 1(c)–1(f) [Figs. 2(c)–2(f)], respectively, considering a 2D (3D) system. Note that in 3D, both the surface and the hinge mode become gapped. The generation of these anomalous dynamical MCMs via our three-step driving protocol is one of the main results of this paper.

III. TOPOLOGICAL CHARACTERIZATION OF FHOTSC PHASE

For the anomalous Floquet phase, the main challenge is to topologically characterize both the zero and π MCMs distinctively. We first pursue the appropriate Wannier sector polarization for 2D FSOTSC and 3D FTOTSC, employing nested Wilson loop techniques [7,18,84], from the Floquet

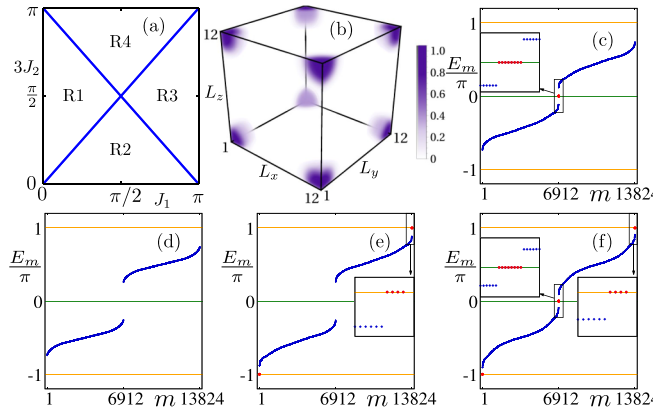

FIG. 2. We repeat the outcome of Fig. 1 considering a 3D cubic lattice of dimension $L_x \times L_y \times L_z$ following Eq. (2). We set $\Delta_1 = \Delta_2 = 1.0$ in the above calculation. The value of the other parameters is chosen to be the same as mentioned in Fig. 1.

operator $U_{d\mathrm{D}}(\mathbf{k},T)$. For 2D FSOTSC (3D FTOTSC), the average first-order (second-order) nested Wannier polarization for the μ'-th (μ''-th) sector $\langle\nu^{\pm\nu_x}_{y,\mathrm{Flq},\mu'}\rangle$ ($\langle\nu^{\pm\nu_y^{\pm\nu_x}}_{z,\mathrm{Flq},\mu''}\rangle$) [84] exhibits a quantized value of 0.5, when the system is in the regime R1 and R3. However, the same is unable to ascertain one whether the modes are lying at the zero or π gap. These nested polarizations reduce to zero for both the trivial phase in R2 and the anomalous phase hosting both zero and π modes in R4.

The inadequacy of the topological invariant, computed from the *quasistatic* Floquet operator, motivates us to hunt for a dynamical topological invariant (both in 2D and 3D) that cannot only extricate R2 from R4 but also unmistakably yield distinct signatures of zero and π modes. We consider the full time evolution operator $U_{d\mathrm{D}}(\mathbf{k},t)$, embodying an *anomalous* periodized part $U_{d\mathrm{D},\epsilon}(\mathbf{k},t)$ and a *normal* quasistatic part $[U(\mathbf{k},T)]^{t/T}_{\epsilon}$, such that [57,64]

$$U_{d\mathrm{D}}(\mathbf{k},t)=U_{d\mathrm{D},\epsilon}(\mathbf{k},t)[U_{d\mathrm{D}}(\mathbf{k},T)]^{t/T}_{\epsilon}, \tag{5}$$

where the subscript ϵ denotes the zero and π gap and enables us to keep track of the origin of the MCMs in these quasienergies. We use the periodized evolution operator (PEO) $U_{d\mathrm{D},\epsilon}(\mathbf{k},t)=U_{d\mathrm{D}}(\mathbf{k},t)[U_{d\mathrm{D}}(\mathbf{k},T)]^{-t/T}_{\epsilon}$ to calculate the pertinent topological invariant. However, unlike $U_{d\mathrm{D}}(\mathbf{k},T)$ the PEO does not possess any conventional band physics and can be gapless at certain time instants [57,64].

In order to capture the nontriviality of the anomalous Floquet modes, we define the dynamical mean polarization as the relative motion of a particle at two instants [64,84]

$$\hat{\bar{x}}(t)=\frac{[\hat{x}(t)+\hat{x}(0)]}{2}, \tag{6}$$

where $\hat{x}(0)=\hat{x}=\sum_{im}\hat{c}^{\dagger}_{im}|0\rangle\, e^{-i\Delta_x x_i}\,\langle 0|\,\hat{c}_{im}$ exemplifies the static polarization [85] with $\Delta_i=2\pi/L_i$, $\hat{x}(t)=U^{\dagger}_{d\mathrm{D},\epsilon}(\mathbf{k},t)\hat{x}\,U_{d\mathrm{D},\epsilon}(\mathbf{k},t)$, and $\hat{c}$'s being the quasiparticle creation operators. The eigenvalue of $\hat{\bar{x}}(t)$ is related to the dynamical Wilson loop operator $W_{x,\epsilon,\mathbf{k}}(t)$ in the following way: $[\hat{\bar{x}}(t)]^{L_x}=\sum_{\mathbf{k}mn}\hat{c}^{\dagger}_{\mathbf{k}m}|0\rangle\,[W_{x,\epsilon,\mathbf{k}}(t)]_{mn}\,\langle 0|\,\hat{c}_{\mathbf{k}n}$. One can find $W_{x,\epsilon,\mathbf{k}}(t)=Q_{x,\epsilon,\mathbf{k}+(L_x-1)\Delta_x\mathbf{e}_x}(t)\cdots Q_{x,\epsilon,\mathbf{k}+\Delta_x\mathbf{e}_x}(t)Q_{x,\epsilon,\mathbf{k}}(t)$ with $Q_{p,\epsilon,\mathbf{k}}(t)=\frac{\mathbb{I}+U^{\dagger}_{d\mathrm{D},\epsilon}(\mathbf{k}+\Delta_p\mathbf{e}_p,t)U_{d\mathrm{D},\epsilon}(\mathbf{k},t)}{2}$, and the unit vector along the pth direction is represented by $\mathbf{e}_p$. From the eigenvalue equation for $W_{x,\epsilon,\mathbf{k}}(t)$, $W_{x,\epsilon,\mathbf{k}}(t)\,|\nu_{x,\epsilon,\mu}(\mathbf{k},t)\rangle=e^{-2\pi i\nu_{x,\epsilon,\mu}(k_{j\neq x},t)}\,|\nu_{x,\epsilon,\mu}(\mathbf{k},t)\rangle$, one obtains the dynamical first-order branches $\nu_{x,\epsilon,\mu}(k_{j\neq x},t)$. Here, $\nu_{x,\epsilon,\mu}(k_{j\neq x},t)$ refers to a relative motion of a particle along the x direction with respect to x_i during $t\in[0,t]$ [64]. These dynamical first-order branches can characterize the anomalous Floquet first-order topological phase. In order to conceive the higher-order moments, one needs to incorporate the nested structure while constructing the Wilson loop, as executed for the static systems with appropriate $Q_{p,\mathbf{k}}$ [7].

To accommodate the FHOTSC phase, the eigenvalues $\nu_{x,\epsilon,\mu}(k_{j\neq x},t)$ remain gapped during the full cycle $t\in[0,T]$ and can be grouped into two separable sets $\pm\nu_{x,\epsilon}$. The dynamical second-order polarization is computed by evaluating the relative motion of a particle along the y direction by projecting onto the set $\pm\nu_{x,\epsilon}$ with projector $P_{\pm\nu_{x,\epsilon}}(t)$ [84]: $\hat{\bar{y}}^{\pm\nu_{x,\epsilon}}(t)=P_{\pm\nu_{x,\epsilon}}(t)\hat{\bar{y}}(t)P_{\pm\nu_{x,\epsilon}}(t)$. Similar to the earlier case, we can obtain a dynamical first-order nested

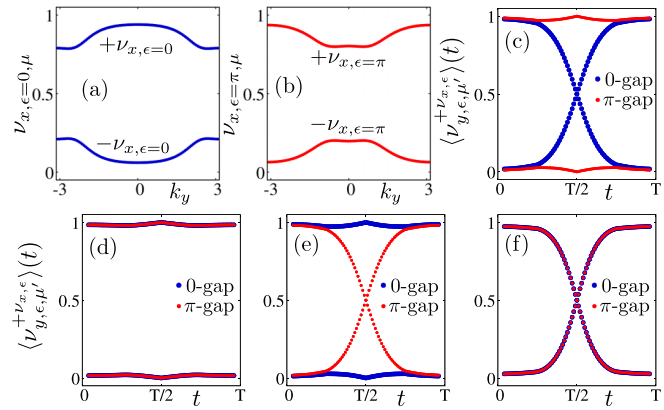

FIG. 3. The gapped dynamical polarization branches $\nu_{x,\epsilon=0,\mu}$ and $\nu_{x,\epsilon=\pi,\mu}$, arising from zero and π gaps, are respectively shown as a function of k_y in (a) and (b), at time $t=\frac{T}{2}$, while the system is in R4. The average quadrupolar motions $\langle\nu^{+\nu_{x,\epsilon,}}_{y,\epsilon,\mu'}\rangle(t)$ for R1–R4 (see Fig. 1) are depicted in (c)–(f), respectively, as a function of time t, manifesting gapless crossing between opposite branches. Here, blue and red dots represent $\langle\nu^{+\nu_{x,\epsilon}}_{y,\epsilon,\mu'}\rangle(t)$ arising from zero and π gaps, respectively. See text for discussion.

Wilson loop operator $W^{\pm\nu_{x,\epsilon}}_{y,\epsilon,\mathbf{k}}(t)$ from $\hat{\bar{y}}^{\pm\nu_{x,\epsilon}}(t)$, $[\hat{\bar{y}}^{\pm\nu_{x,\epsilon}}(t)]^{L_y}=\sum_{\mathbf{k},\mu_1,\mu_2\in\pm\nu_{x,\epsilon}}\gamma^{\dagger}_{\mathbf{k}\epsilon\mu_1}(t)\,|0\rangle\,[W^{\pm\nu_{x,\epsilon}}_{y,\epsilon,\mathbf{k}}(t)]_{\mu_1\mu_2}\,\langle 0|\,\gamma_{\mathbf{k}\epsilon\mu_2}(t)$, where γ's are constituted from $|\nu_{x,\epsilon,\mu}(\mathbf{k},t)\rangle$ according to the projection rule [84]. This leads to $W^{\pm\nu_{x,\epsilon}}_{y,\epsilon,\mathbf{k}}(t)=Q^{\pm\nu_{x,\epsilon}}_{y,\epsilon,\mathbf{k}+(L_y-1)\Delta_y\mathbf{e}_y}(t)\cdots Q^{\pm\nu_{x,\epsilon}}_{y,\epsilon,\mathbf{k}+\Delta_y\mathbf{e}_y}(t)Q^{\pm\nu_{x,\epsilon}}_{y,\epsilon,\mathbf{k}}(t)$ with $[Q^{\pm\nu_{x,\epsilon}}_{y,\epsilon,\mathbf{k}}(t)]_{\mu_1\mu_2}=\sum_{mn}[\nu_{x,\epsilon,\mu_1}(\mathbf{k}+\Delta_y\mathbf{e}_y,t)]^{*}_{m}\,[Q_{y,\epsilon,\mathbf{k}}(t)]_{mn}[\nu_{x,\epsilon,\mu_2}(\mathbf{k},t)]_{n}$. The dynamical second-order quadrupolar branches $\nu^{\pm\nu_{x,\epsilon}}_{y,\epsilon,\mu'}(k_{j\neq y},t)$ can be obtained from the eigenvalue equation $W^{\pm\nu_{x,\epsilon}}_{y,\epsilon,\mathbf{k}}(t)\,|\nu^{\pm\nu_{x,\epsilon}}_{y,\epsilon,\mu'}(\mathbf{k},t)\rangle=e^{-2\pi i\nu^{\pm\nu_{x,\epsilon}}_{y,\epsilon,\mu'}(k_{j\neq y},t)}\,|\nu^{\pm\nu_{x,\epsilon}}_{y,\epsilon,\mu'}(\mathbf{k},t)\rangle$. These quadrupolar branches can topologically characterize the anomalous 2D FSOTSC, which we illustrate in Fig. 3.

Proceeding further, the octupolar phase guarantees gapped quadrupolar branches during time $t\in[0,T]$ and thus can be grouped into two dissociable sets $\pm\nu^{\pm\nu_{x,\epsilon}}_{y,\epsilon}$. The dynamical third-order polarization can be portrayed as the relative motion of a particle along the remaining z direction using the projector $P_{\pm\nu^{\pm\nu_{x,\epsilon}}_{y,\epsilon}}(t)$ onto $\pm\nu^{\pm\nu_{x,\epsilon}}_{y,\epsilon}$: $\hat{\bar{z}}^{\pm\nu^{\pm\nu_{x,\epsilon}}_{y,\epsilon}}(t)=P_{\pm\nu^{\pm\nu_{x,\epsilon}}_{y,\epsilon}}(t)\hat{\bar{z}}(t)P_{\pm\nu^{\pm\nu_{x,\epsilon}}_{y,\epsilon}}(t)$ [84]. Following a similar line of argument, the dynamical second-order nested Wilson loop operator is found to be $[\hat{\bar{z}}^{\pm\nu^{\pm\nu_{x,\epsilon}}_{y,\epsilon}}(t)]^{L_z}=\sum_{\mathbf{k},\mu'_1,\mu'_2\in\pm\nu^{\pm\nu_{x,\epsilon}}_{y,\epsilon}}\eta^{\dagger}_{\mathbf{k}\epsilon\mu'_1}(t)\,|0\rangle\,[W^{\pm\nu^{\pm\nu_{x,\epsilon}}_{y,\epsilon}}_{z,\epsilon,\mathbf{k}}(t)]_{\mu'_1\mu'_2}\,\langle 0|\,\eta_{\mathbf{k}\epsilon\mu'_2}(t)$, where η's are comprised from $|\nu_{x,\epsilon,\mu}(\mathbf{k},t)\rangle$ and $|\nu^{\pm\nu_{x,\epsilon}}_{y,\epsilon,\mu'}(\mathbf{k},t)\rangle$ [84]. We therefore obtain $W^{\pm\nu^{\pm\nu_{x,\epsilon}}_{y,\epsilon}}_{z,\epsilon,\mathbf{k}}(t)=Q^{\pm\nu^{\pm\nu_{x,\epsilon}}_{y,\epsilon}}_{z,\epsilon,\mathbf{k}+(L_z-1)\Delta_z\mathbf{e}_z}(t)\cdots Q^{\pm\nu^{\pm\nu_{x,\epsilon}}_{y,\epsilon}}_{z,\epsilon,\mathbf{k}+\Delta_z\mathbf{e}_z}(t)Q^{\pm\nu^{\pm\nu_{x,\epsilon}}_{y,\epsilon}}_{z,\epsilon,\mathbf{k}}(t)$, with $[Q^{\pm\nu^{\pm\nu_{x,\epsilon}}_{y,\epsilon}}_{z,\epsilon,\mathbf{k}}(t)]_{\mu'_1\mu'_2}=\sum_{mn\mu_1\mu_2}[\nu^{\pm\nu_{x,\epsilon}}_{y,\epsilon,\mu'_1}(\mathbf{k}+\Delta_z\mathbf{e}_z,t)]^{*}_{\mu_1}\,[\nu_{x,\epsilon,\mu_1}(\mathbf{k}+\Delta_z\mathbf{e}_z,t)]^{*}_{m}[Q_{z,\epsilon,\mathbf{k}}(t)]_{mn}[\nu_{x,\epsilon,\mu_2}(\mathbf{k},t)]_{n}\,[\nu^{\pm\nu_{x,\epsilon}}_{y,\epsilon,\mu'_2}(\mathbf{k},t)]_{\mu_2}$. From the eigenvalue of $W^{\pm\nu^{\pm\nu_{x,\epsilon}}_{y,\epsilon}}_{z,\epsilon,\mathbf{k}}(t)$, we procure the dynamical third-order octupolar branch as

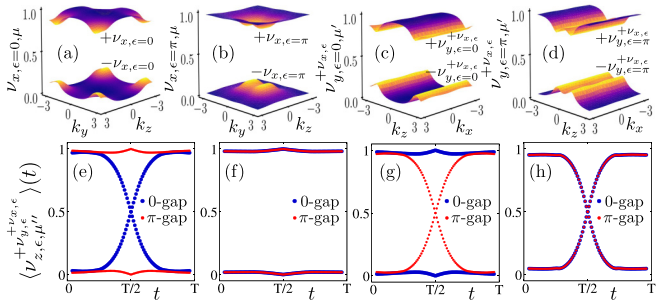

FIG. 4. We repeat Figs. 3(a) and 3(b) for the 3D cubic lattice as a function of k_z, k_x and depict them in (a) and (b), respectively. The gapped dynamical quadrupolar branches $\nu^{+\nu_{x,\epsilon}}_{y,\epsilon=0,\mu'}$ and $\nu^{+\nu_{x,\epsilon}}_{y,\epsilon=\pi,\mu'}$ are shown in (c) and (d), respectively, at $t=\frac{T}{2}$ in R4. The average octupolar motions $\langle \nu^{+\nu_{y,\epsilon}}_{z,\epsilon,\mu''}\rangle(t)$ for R1–R4 are shown in (c)–(f), respectively, indicating the gapless crossing between opposite branches. Here, blue and red dots represent $\langle \nu^{+\nu_{y,\epsilon}}_{z,\epsilon,\mu''}\rangle(t)$ arising from zero and π gaps, respectively and are discussed in the text.

$\nu^{\pm\nu_{y,\epsilon}}_{z,\epsilon,\mu''}(k_{j\neq z},t)$ that is adopted to topologically characterize the 3D FTOTSC as demonstrated in Fig. 4.

A. Dynamical quadrupole moment

Limited to 2D, the mirror symmetry $\mathcal{M}_x$ enforces $\nu_{x,\epsilon,\mu}(k_y,t)$ to appear in pairs: $\nu_{x,\epsilon,\mu_1}(k_y,t)=-\nu_{x,\epsilon,\mu_2}(k_y,t)$, with $\mu_1\in+\nu_{x,\epsilon,\mu}$ and $\mu_2\in-\nu_{x,\epsilon,\mu}$. Moreover, $\mathcal{M}_y$ compels $\nu_{x,\epsilon,\mu}(k_y,t)=\nu_{x,\epsilon,\mu}(-k_y,t)$ within each branch μ [64]. We show these behaviors in Figs. 3(a) and 3(b) for zero and π gaps at $t=\frac{T}{2}$, respectively, when the system is in R4. $\mathcal{M}_x$ imposes the quadrupolar branches, derived from opposite first-order branches, to be the same, i.e., $\nu^{+\nu_{x,\epsilon}}_{y,\epsilon,\mu'}(k_x,t)=\nu^{-\nu_{x,\epsilon}}_{y,\epsilon,\mu'}(k_x,t)$, and $\mathcal{M}_y$ causes the quadrupolar branches to appear in pairs: $\nu^{+\nu_{x,\epsilon}}_{y,\epsilon,\mu'_1}(k_x,t)=-\nu^{+\nu_{x,\epsilon}}_{y,\epsilon,\mu'_2}(k_x,t)$ [64]. It is evident from the above discussion that the mirror symmetries do not impose any constraints on the quantization of the quadrupolar branches at any time instant t, unlike the static case where ν's are allowed to take values of either zero or 1/2 (mod 1) [7].

The average quadrupolar motion $\langle\nu^{+\nu_{x,\epsilon}}_{y,\epsilon,\mu'}\rangle(t)=\frac{1}{L_x}\sum_{k_x}\nu^{+\nu_{x,\epsilon}}_{y,\epsilon,\mu'}(k_x,t)$, however, plays a paramount role in understanding the topological Floquet modes. Now, $U_{2D,\epsilon}(0)=U_{2D,\epsilon}(T)=\mathbb{I}$ necessitates the particles to undergo a round trip during the time interval $t\in[0,T]$ and enforces $\langle\nu^{+\nu_{x,\epsilon}}_{y,\epsilon,\mu'}\rangle(t=0)=\langle\nu^{+\nu_{x,\epsilon}}_{y,\epsilon,\mu'}\rangle(t=T)=0 \pmod 1$ to be the fixed points. For a topologically trivial phase, $\langle\nu^{+\nu_{x,\epsilon}}_{y,\epsilon,\mu'}\rangle(0)$ and $\langle\nu^{+\nu_{x,\epsilon}}_{y,\epsilon,\mu'}\rangle(T)$ are adiabatically connected without any gap closing between two branches $\forall t\in[0,T]$ [see Fig. 3(c) for π gap, Fig. 3(d) for both gaps, and Fig. 3(e) for zero gap]. The presence of MCMs (see Fig. 1) in the gap ϵ, obstructs the motion of $\langle\nu^{+\nu_{x,\epsilon}}_{y,\epsilon,\mu'}\rangle(t)$ in the time interval $t\in[0,T]$ and two branches cross each other at $\frac{1}{2}\pmod 1$ at $t=\frac{T}{2}$ [see Fig. 3(c) for zero gap, Fig. 3(e) for π gap, and Fig. 3(f) for both zero and π gaps). We thus obtain the quantization of the dynamical quadrupole moment $Q^{+\nu_{x,\epsilon}}_{\epsilon}=\int_0^T dt\,\partial_t\langle\nu^{+\nu_{x,\epsilon}}_{y,\epsilon,\mu'}\rangle(t)=(0)\ 1 \pmod 1$, for the (trivial) topological case, giving rise to a $\mathbb{Z}_2$ classification. Thus, the generalization of the dynamical quadrupole moment for the 2D FSOTSC (with an eight-band model) is another important result of this paper.

B. Dynamical octupole moment

In 3D, $\mathcal{M}_x$ seeks $\nu_{x,\epsilon,\mu_1}(k_y,k_z,t)=-\nu_{x,\epsilon,\mu_2}(k_y,k_z,t)$, with $\mu_1\in+\nu_{x,\epsilon,\mu}$ and $\mu_2\in-\nu_{x,\epsilon,\mu}$, while $\mathcal{M}_y$ and $\mathcal{M}_z$ set the shape of the branch such that $\nu_{x,\epsilon,\mu}(k_y,k_z,t)=\nu_{x,\epsilon,\mu}(-k_y,k_z,t)$ and $\nu_{x,\epsilon,\mu}(k_y,k_z,t)=\nu_{x,\epsilon,\mu}(k_y,-k_z,t)$ within each branch μ. We demonstrate the dynamical first-order branch in Figs. 4(a) and 4(b) while the system is in R4 at $t=\frac{T}{2}$ for the zero and π gaps, respectively. Here, $\mathcal{M}_x$ invokes second-order branches calculated from opposite first-order branches $\pm\nu_{x,\epsilon,\mu}(k_y,k_z,t)$ to be identical, $\mathcal{M}_y$ requires $\nu^{+\nu_{x,\epsilon}}_{y,\epsilon,\mu'_1}(k_z,k_x,t)=-\nu^{+\nu_{x,\epsilon}}_{y,\epsilon,\mu'_2}(k_z,k_x,t)$, and $\mathcal{M}_z$ enforces $\nu^{+\nu_{x,\epsilon}}_{y,\epsilon,\mu'}(k_z,k_x,t)=\nu^{+\nu_{x,\epsilon}}_{y,\epsilon,\mu'}(-k_z,k_x,t)$. We depict the dynamical second-order branch in Figs. 4(c) and 4(d) for zero and π gaps, respectively, at $t=\frac{T}{2}$, while the system is in R4. Akin to the first-order branches, the quadrupolar branches also exhibit a finite gap and set the stage for the calculation of the third-order (octupolar) dynamical branch. Here, $\mathcal{M}_x$ and $\mathcal{M}_y$ ensure the octupolar branch calculated from different quadrupolar branches to remain the same and $\mathcal{M}_z$ compels the octupolar branch to appear in pairs: $\nu^{+\nu_{y,\epsilon}}_{z,\epsilon,\mu''_1}(k_x,k_y,t)=-\nu^{+\nu_{y,\epsilon}}_{z,\epsilon,\mu''_2}(k_x,k_y,t)$.

Following the 2D case, we introduce the average octupolar motion as $\langle\nu^{+\nu_{y,\epsilon}}_{z,\epsilon,\mu''}\rangle(t)=\frac{1}{L_xL_y}\sum_{k_xk_y}\nu^{+\nu_{y,\epsilon}}_{z,\epsilon,\mu''}(k_x,k_y,t)$. For the trivial case, $\langle\nu^{+\nu_{y,\epsilon}}_{z,\epsilon,\mu''}\rangle(t:0\to T)$ winds back to the original value (mod 1) without experiencing any gap closing among the branches [see Fig. 4(e) for π gap, Fig. 4(f) both zero and π gaps, and Fig. 4(g) for zero gap]. The topologically nontrivial situation refers to a gap closing of two different octupolar branches at $\frac{1}{2}\pmod 1$ when $\langle\nu^{+\nu_{y,\epsilon}}_{z,\epsilon,\mu''}\rangle(t\to 0)=0\ (1)$ evolves to $\langle\nu^{+\nu_{y,\epsilon}}_{z,\epsilon,\mu''}\rangle(t\to T)=1\ (0)$ as depicted in Fig. 4(e) for zero gap, Fig. 4(g) for π gap, and Fig. 4(h) for both zero and π gaps. Hence, the notion of a $\mathbb{Z}_2$ invariant works for the 3D octupole moment similar to the 2D quadrupolar moment: $O^{+\nu_{y,\epsilon}}_{\epsilon}=\int_0^T dt\,\partial_t\langle\nu^{+\nu_{y,\epsilon}}_{z,\epsilon,\mu''}\rangle(t)=(0)\ 1 \pmod 1$, for the (trivial) topological case. We emphasize that the topological characterization of anomalous MCMs $(0-\pi)$ via the dynamical octupole moment in the FTOTSC phase is the prime result of this paper.

IV. SUMMARY AND CONCLUSIONS

To summarize, in this paper, we prescribe a step-drive protocol to dynamically construct 2D FSOTSC and 3D FTOTSC hosting 0D MCMs. Exploiting the phase diagrams, we illustrate the emergence of both regular zero and anomalous π MCMs separately and simultaneously. We circumvent the elusive affair of complete topological characterization for available dynamical phases by analyzing PEO in both 2D and 3D. This allows us to tie up the dynamical quadrupole and octupole moments with $\mathbb{Z}_2$ classifications and enables us to topologically characterize the FHOTSC phases. Along

this direction, the stability of these dynamic phases in the presence of strong disorder might also be an intriguing future direction.

Note that the Majorana-based qubit architectures have been studied for FSOTSC, hosting both zero and anomalous π modes, in the context of fault-tolerant quantum computing [78]. We believe that the spatially separated MCMs in FTOTSC, observed for the present case, can become potentially useful for further extensions of the quantum gate operations in 3D. The three-step periodic driving protocol implemented here is found to be very convenient for the model-based studies [64]. Given the experimental advancement in Floquet driving [86–88] and HOT phases [89–91], our proposal carries possible implications of practical relevance [92]. However, from the experimental viewpoint, the engineering of HOT phases employing laser drive/light fields can be more realistic, which we leave for future investigations and will be presented elsewhere. We believe that the present scheme of topological characterization would work for continuous time driving.

ACKNOWLEDGMENT

A.K.G. and A.S. acknowledge SAMKHYA: High-Performance Computing Facility provided by Institute of Physics, Bhubaneswar, for numerical computations.

[1] A. Yu. Kitaev, Unpaired Majorana fermions in quantum wires, Phys.-Usp. **44**, 131 (2001).
[2] D. A. Ivanov, Non-Abelian Statistics of Half-Quantum Vortices in p-Wave Superconductors, Phys. Rev. Lett. **86**, 268 (2001).
[3] C. Nayak, S. H. Simon, A. Stern, M. Freedman, and S. Das Sarma, Non-Abelian anyons and topological quantum computation, Rev. Mod. Phys. **80**, 1083 (2008).
[4] X.-L. Qi and S.-C. Zhang, Topological insulators and superconductors, Rev. Mod. Phys. **83**, 1057 (2011).
[5] L. Fu and C. L. Kane, Superconducting Proximity Effect and Majorana Fermions at the Surface of a Topological Insulator, Phys. Rev. Lett. **100**, 096407 (2008).
[6] W. A. Benalcazar, B. A. Bernevig, and T. L. Hughes, Quantized electric multipole insulators, Science **357**, 61 (2017).
[7] W. A. Benalcazar, B. A. Bernevig, and T. L. Hughes, Electric multipole moments, topological multipole moment pumping, and chiral hinge states in crystalline insulators, Phys. Rev. B **96**, 245115 (2017).
[8] Z. Song, Z. Fang, and C. Fang, $(d-2)$-Dimensional Edge States of Rotation Symmetry Protected Topological States, Phys. Rev. Lett. **119**, 246402 (2017).
[9] J. Langbehn, Y. Peng, L. Trifunovic, F. von Oppen, and P. W. Brouwer, Reflection-Symmetric Second-Order Topological Insulators and Superconductors, Phys. Rev. Lett. **119**, 246401 (2017).
[10] F. Schindler, A. M. Cook, M. G. Vergniory, Z. Wang, S. S. P. Parkin, B. A. Bernevig, and T. Neupert, Higher-order topological insulators, Sci. Adv. **4**, eaat0346 (2018).
[11] S. Franca, J. van den Brink, and I. C. Fulga, An anomalous higher-order topological insulator, Phys. Rev. B **98**, 201114(R) (2018).
[12] Z. Wang, B. J. Wieder, J. Li, B. Yan, and B. A. Bernevig, Higher-Order Topology, Monopole Nodal Lines, and the Origin of Large Fermi Arcs in Transition Metal Dichalcogenides $x\mathrm{Te}_2$ (x = Mo, W), Phys. Rev. Lett. **123**, 186401 (2019).
[13] M. Ezawa, Higher-Order Topological Insulators and Semimetals on the Breathing Kagome and Pyrochlore Lattices, Phys. Rev. Lett. **120**, 026801 (2018).
[14] D. Călugăru, V. Juričić, and B. Roy, Higher-order topological phases: A general principle of construction, Phys. Rev. B **99**, 041301(R) (2019).
[15] L. Trifunovic and P. W. Brouwer, Higher-Order Bulk-Boundary Correspondence for Topological Crystalline Phases, Phys. Rev. X **9**, 011012 (2019).
[16] E. Khalaf, Higher-order topological insulators and superconductors protected by inversion symmetry, Phys. Rev. B **97**, 205136 (2018).
[17] P. Szumniak, D. Loss, and J. Klinovaja, Hinge modes and surface states in second-order topological three-dimensional quantum Hall systems induced by charge density modulation, Phys. Rev. B **102**, 125126 (2020).
[18] X. Ni, M. Li, M. Weiner, A. Alù, and A. B. Khanikaev, Demonstration of a quantized acoustic octupole topological insulator, Nat. Commun. **11**, 2108 (2020).
[19] B. Xie, H. X. Wang, X. Zhang, P. Zhan, J. H. Jiang, M. Lu, and Y. Chen, Higher-order band topology, Nat. Rev. Phys. **3**, 520 (2021).
[20] M. Geier, L. Trifunovic, M. Hoskam, and P. W. Brouwer, Second-order topological insulators and superconductors with an order-two crystalline symmetry, Phys. Rev. B **97**, 205135 (2018).
[21] X. Zhu, Tunable Majorana corner states in a two-dimensional second-order topological superconductor induced by magnetic fields, Phys. Rev. B **97**, 205134 (2018).
[22] T. Liu, J. J. He, and F. Nori, Majorana corner states in a two-dimensional magnetic topological insulator on a high-temperature superconductor, Phys. Rev. B **98**, 245413 (2018).
[23] Z. Yan, F. Song, and Z. Wang, Majorana Corner Modes in a High-Temperature Platform, Phys. Rev. Lett. **121**, 096803 (2018).
[24] Y. Wang, M. Lin, and T. L. Hughes, Weak-pairing higher order topological superconductors, Phys. Rev. B **98**, 165144 (2018).
[25] C. Zeng, T. D. Stanescu, C. Zhang, V. W. Scarola, and S. Tewari, Majorana Corner Modes with Solitons in an Attractive Hubbard-Hofstadter Model of Cold Atom Optical Lattices, Phys. Rev. Lett. **123**, 060402 (2019).
[26] R.-X. Zhang, W. S. Cole, and S. Das Sarma, Helical Hinge Majorana Modes in Iron-Based Superconductors, Phys. Rev. Lett. **122**, 187001 (2019).
[27] R.-X. Zhang, W. S. Cole, X. Wu, and S. Das Sarma, Higher-Order Topology and Nodal Topological Superconductivity in Fe(Se,Te) Heterostructures, Phys. Rev. Lett. **123**, 167001 (2019).
[28] Y. Volpez, D. Loss, and J. Klinovaja, Second-Order Topological Superconductivity in π-Junction Rashba Layers, Phys. Rev. Lett. **122**, 126402 (2019).

[29] Z. Yan, Majorana corner and hinge modes in second-order topological insulator/superconductor heterostructures, Phys. Rev. B **100**, 205406 (2019).
[30] S. A. A. Ghorashi, X. Hu, T. L. Hughes, and E. Rossi, Second-order Dirac superconductors and magnetic field induced Majorana hinge modes, Phys. Rev. B **100**, 020509(R) (2019).
[31] S. A. A. Ghorashi, T. L. Hughes, and E. Rossi, Vortex and Surface Phase Transitions in Superconducting Higher-order Topological Insulators, Phys. Rev. Lett. **125**, 037001 (2020).
[32] Y.-J. Wu, J. Hou, Y.-M. Li, X.-W. Luo, X. Shi, and C. Zhang, In-Plane Zeeman-Field-Induced Majorana Corner and Hinge Modes in an *s*-Wave Superconductor Heterostructure, Phys. Rev. Lett. **124**, 227001 (2020).
[33] K. Laubscher, D. Chughtai, D. Loss, and J. Klinovaja, Kramers pairs of Majorana corner states in a topological insulator bilayer, Phys. Rev. B **102**, 195401 (2020).
[34] B. Roy, Higher-order topological superconductors in $\mathcal{P}$-, $\mathcal{T}$-odd quadrupolar Dirac materials, Phys. Rev. B **101**, 220506(R) (2020).
[35] S.-B. Zhang and B. Trauzettel, Detection of second-order topological superconductors by Josephson junctions, Phys. Rev. Research **2**, 012018(R) (2020).
[36] S.-B. Zhang, W. B. Rui, A. Calzona, S.-J. Choi, A. P. Schnyder, and B. Trauzettel, Topological and holonomic quantum computation based on second-order topological superconductors, Phys. Rev. Research **2**, 043025 (2020).
[37] S.-B. Zhang, A. Calzona, and B. Trauzettel, All-electrically tunable networks of Majorana bound states, Phys. Rev. B **102**, 100503(R) (2020).
[38] M. Kheirkhah, Z. Yan, and F. Marsiglio, Vortex-line topology in iron-based superconductors with and without second-order topology, Phys. Rev. B **103**, L140502 (2021).
[39] K. Plekhanov, N. Müller, Y. Volpez, D. M. Kennes, H. Schoeller, D. Loss, and J. Klinovaja, Quadrupole spin polarization as signature of second-order topological superconductors, Phys. Rev. B **103**, L041401 (2021).
[40] A. Tiwari, A. Jahin, and Y. Wang, Chiral Dirac superconductors: Second-order and boundary-obstructed topology, Phys. Rev. Research **2**, 043300 (2020).
[41] Z. Yan, Higher-Order Topological Odd-Parity Superconductors, Phys. Rev. Lett. **123**, 177001 (2019).
[42] J. Ahn and B.-J. Yang, Higher-order topological superconductivity of spin-polarized fermions, Phys. Rev. Research **2**, 012060(R) (2020).
[43] X.-J. Luo, X.-H. Pan, and X. Liu, Higher-order topological superconductors based on weak topological insulators, Phys. Rev. B **104**, 104510 (2021).
[44] Q. Wang, C.-C. Liu, Y.-M. Lu, and F. Zhang, High-Temperature Majorana Corner States, Phys. Rev. Lett. **121**, 186801 (2018).
[45] A. K. Ghosh, T. Nag, and A. Saha, Hierarchy of higher-order topological superconductors in three dimensions, Phys. Rev. B **104**, 134508 (2021).
[46] B. Roy and V. Juričić, Mixed-parity octupolar pairing and corner Majorana modes in three dimensions, Phys. Rev. B **104**, L180503 (2021).
[47] Y. Kayanuma and K. Saito, Coherent destruction of tunneling, dynamic localization, and the Landau-Zener formula, Phys. Rev. A **77**, 010101(R) (2008).
[48] T. Nag, S. Roy, A. Dutta, and D. Sen, Dynamical localization in a chain of hard core bosons under periodic driving, Phys. Rev. B **89**, 165425 (2014).
[49] T. Nag, D. Sen, and A. Dutta, Maximum group velocity in a one-dimensional model with a sinusoidally varying staggered potential, Phys. Rev. A **91**, 063607 (2015).
[50] L. D'Alessio and A. Polkovnikov, Many-body energy localization transition in periodically driven systems, Ann. Phys. **333**, 19 (2013).
[51] L. D'Alessio and M. Rigol, Long-time Behavior of Isolated Periodically Driven Interacting Lattice Systems, Phys. Rev. X **4**, 041048 (2014).
[52] P. Ponte, A. Chandran, Z. Papić, and D. A. Abanin, Periodically driven ergodic and many-body localized quantum systems, Ann. Phys. **353**, 196 (2015).
[53] D. V. Else, B. Bauer, and C. Nayak, Floquet Time Crystals, Phys. Rev. Lett. **117**, 090402 (2016).
[54] V. Khemani, A. Lazarides, R. Moessner, and S. L. Sondhi, Phase Structure of Driven Quantum Systems, Phys. Rev. Lett. **116**, 250401 (2016).
[55] T. Nag, R.-J. Slager, T. Higuchi, and T. Oka, Dynamical synchronization transition in interacting electron systems, Phys. Rev. B **100**, 134301 (2019).
[56] T. N. Ikeda, K. Chinzei, and H. Tsunetsugu, Floquet-theoretical formulation and analysis of high-order harmonic generation in solids, Phys. Rev. A **98**, 063426 (2018).
[57] M. S. Rudner, N. H. Lindner, E. Berg, and M. Levin, Anomalous Edge States and the Bulk-Edge Correspondence for Periodically Driven Two-Dimensional Systems, Phys. Rev. X **3**, 031005 (2013).
[58] R. W. Bomantara, L. Zhou, J. Pan, and J. Gong, Coupled-wire construction of static and Floquet second-order topological insulators, Phys. Rev. B **99**, 045441 (2019).
[59] T. Nag, V. Juričić, and B. Roy, Out of equilibrium higher-order topological insulator: Floquet engineering and quench dynamics, Phys. Rev. Research **1**, 032045(R) (2019).
[60] Y. Peng and G. Refael, Floquet Second-Order Topological Insulators from Nonsymmorphic Space-Time Symmetries, Phys. Rev. Lett. **123**, 016806 (2019).
[61] R. Seshadri, A. Dutta, and D. Sen, Generating a second-order topological insulator with multiple corner states by periodic driving, Phys. Rev. B **100**, 115403 (2019).
[62] M. Rodriguez-Vega, A. Kumar, and B. Seradjeh, Higher-order Floquet topological phases with corner and bulk bound states, Phys. Rev. B **100**, 085138 (2019).
[63] A. K. Ghosh, G. C. Paul, and A. Saha, Higher order topological insulator via periodic driving, Phys. Rev. B **101**, 235403 (2020).
[64] B. Huang and W. V. Liu, Floquet Higher-Order Topological Insulators with Anomalous Dynamical Polarization, Phys. Rev. Lett. **124**, 216601 (2020).
[65] H. Hu, B. Huang, E. Zhao, and W. V. Liu, Dynamical Singularities of Floquet Higher-Order Topological Insulators, Phys. Rev. Lett. **124**, 057001 (2020).
[66] Y. Peng, Floquet higher-order topological insulators and superconductors with space-time symmetries, Phys. Rev. Research **2**, 013124 (2020).
[67] T. Nag, V. Juričić, and B. Roy, Hierarchy of higher-order Floquet topological phases in three dimensions, Phys. Rev. B **103**, 115308 (2021).

[68] R.-X. Zhang and Z.-C. Yang, Tunable fragile topology in Floquet systems, Phys. Rev. B **103**, L121115 (2021).
[69] R. V. Bhat and S. Bera, Out of equilibrium chiral higher order topological insulator on a π-flux square lattice, J. Phys.: Condens. Matter **33**, 164005 (2021).
[70] W. Zhu, Y. D. Chong, and J. Gong, Floquet higher-order topological insulator in a periodically driven bipartite lattice, Phys. Rev. B **103**, L041402 (2021).
[71] S. Chaudhary, A. Haim, Y. Peng, and G. Refael, Phonon-induced Floquet topological phases protected by space-time symmetries, Phys. Rev. Research **2**, 043431 (2020).
[72] J. Yu, R.-X. Zhang, and Z.-D. Song, Dynamical symmetry indicators for Floquet crystals, Nat. Commun. **12**, 5985 (2021).
[73] D. Vu, Dynamic bulk-boundary correspondence for anomalous Floquet topology, Phys. Rev. B **105**, 064304 (2022).
[74] A. K. Ghosh, T. Nag, and A. Saha, Systematic generation of the cascade of anomalous dynamical first and higher-order modes in Floquet topological insulators, Phys. Rev. B **105**, 115418 (2022).
[75] X.-L. Du, R. Chen, R. Wang, and D.-H. Xu, Weyl nodes with higher-order topology in an optically driven nodal-line semimetal, Phys. Rev. B **105**, L081102 (2022).
[76] Z. Ning, B. Fu, D.-H. Xu, and R. Wang, Tailoring quadrupole topological insulators with periodic driving and disorder, arXiv:2201.02414.
[77] K. Plekhanov, M. Thakurathi, D. Loss, and J. Klinovaja, Floquet second-order topological superconductor driven via ferromagnetic resonance, Phys. Rev. Research **1**, 032013(R) (2019).
[78] R. W. Bomantara and J. Gong, Measurement-only quantum computation with Floquet Majorana corner modes, Phys. Rev. B **101**, 085401 (2020).
[79] R. W. Bomantara, Time-induced second-order topological superconductors, Phys. Rev. Research **2**, 033495 (2020).
[80] A. K. Ghosh, T. Nag, and A. Saha, Floquet generation of a second-order topological superconductor, Phys. Rev. B **103**, 045424 (2021).
[81] A. K. Ghosh, T. Nag, and A. Saha, Floquet second order topological superconductor based on unconventional pairing, Phys. Rev. B **103**, 085413 (2021).
[82] D. Vu, R.-X. Zhang, Z.-C. Yang, and S. Das Sarma, Superconductors with anomalous Floquet higher-order topology, Phys. Rev. B **104**, L140502 (2021).
[83] B. Roy, S. Ali Akbar Ghorashi, M. S. Foster, and A. H. Nevidomskyy, Topological superconductivity of spin-3/2 carriers in a three-dimensional doped Luttinger semimetal, Phys. Rev. B **99**, 054505 (2019).
[84] See Supplemental Material at http://link.aps.org/supplemental/10.1103/PhysRevB.105.155406 for detailed construction of the Floquet operator and the periodized evolution operator, elaborated formalism for computing the dynamical multipole moments, calculation for quasi-static multipole moments, and generation of Floquet second-order topological superconductor.
[85] R. Resta, Quantum-Mechanical Position Operator in Extended Systems, Phys. Rev. Lett. **80**, 1800 (1998).
[86] Y. H. Wang, H. Steinberg, P. Jarillo-Herrero, and N. Gedik, Observation of Floquet-Bloch states on the surface of a topological insulator, Science **342**, 453 (2013).
[87] Y.-G. Peng, C.-Z. Qin, D.G. Zhao, Y. X. Shen, X.-Y. Xu, M. Bao, H. Jia, and X.-F. Zhu, Experimental demonstration of anomalous Floquet topological insulator for sound, Nat. Commun. **7**, 13368 (2016).
[88] L. J. Maczewsky, J. M. Zeuner, S. Nolte, and A. Szameit, Observation of photonic anomalous Floquet topological insulators, Nat. Commun. **8**, 13756 (2017).
[89] M. Serra-Garcia, V. Peri, R. Süsstrunk, O. R. Bilal, T. Larsen, L. G. Villanueva, and S. D. Huber, Observation of a phononic quadrupole topological insulator, Nature (London) **555**, 342 (2018).
[90] F. Schindler, Z. Wang, M. G. Vergniory, A. M. Cook, A. Murani, S. Sengupta, A. Y. Kasumov, R. Deblock, S. Jeon, I. Drozdov *et al.*, Higher-order topology in bismuth, Nat. Phys. **14**, 918 (2018).
[91] H. Xue, Y. Yang, F. Gao, Y. Chong, and B. Zhang, Acoustic higher-order topological insulator on a kagome lattice, Nat. Mater. **18**, 108 (2019).
[92] W. Zhu, H. Xue, J. Gong, Y. Chong, and B. Zhang, Time-periodic corner states from Floquet higher-order topology, Nat. Commun. **13**, 11 (2022).